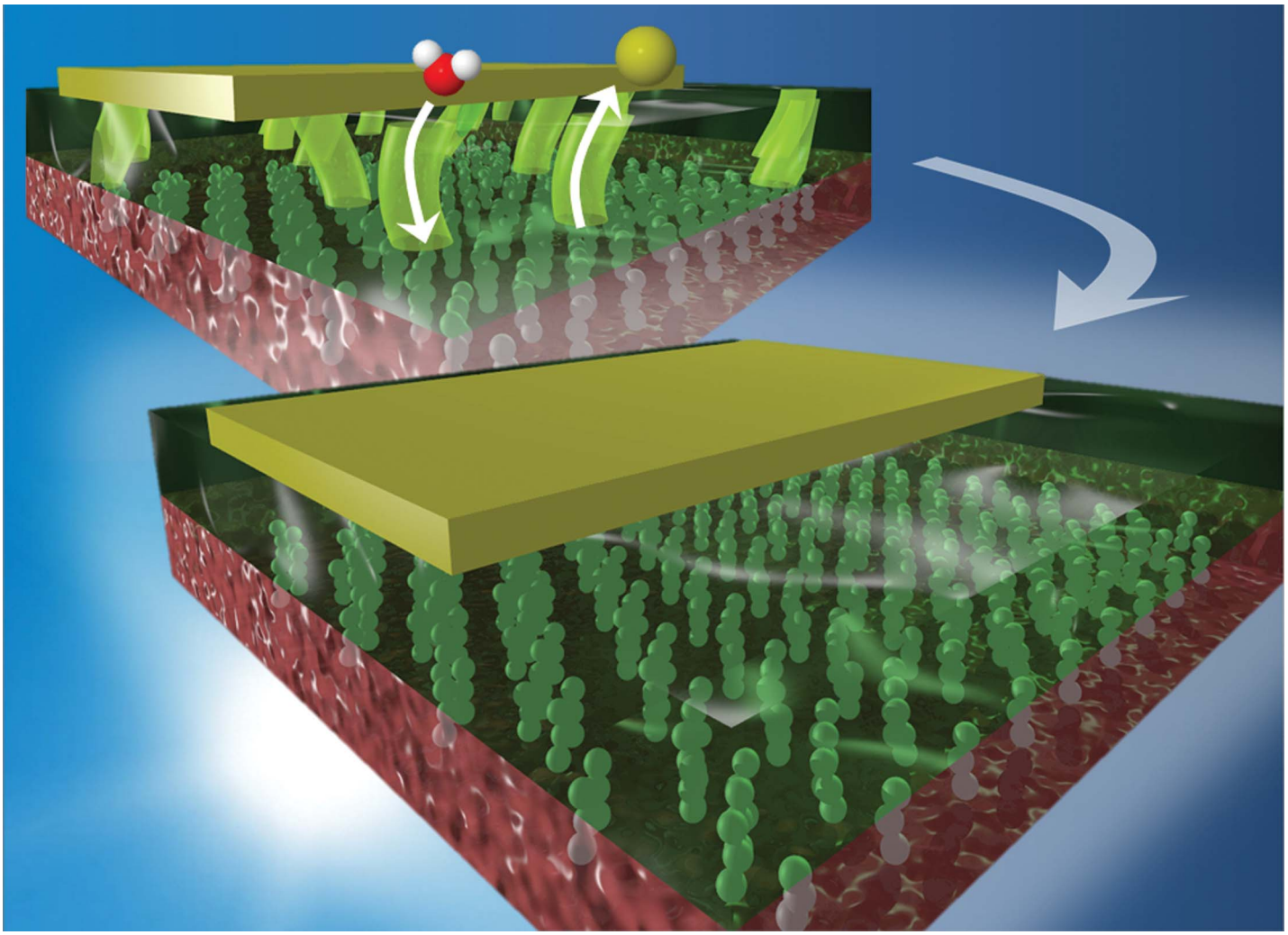

Showcasing the influences of pinholes in hole transport layers on the stability of perovskite solar cells by Prof. Yabing Qi at the Energy Materials and Surface Sciences Unit in Okinawa Institute of Science and Technology Graduate University.

Title: Pinhole-free hole transport layers significantly improve the stability of $MAPbI_3$-based perovskite solar cells under operating conditions

Pinholes accelerate inward-diffusion of gas molecules from ambient air leading to degradation of perovskite underneath the pinhole containing spiro-MeOTAD hole transport layer. A new method has been developed to deposit pinhole-free spiro-MeOTAD hole transport layers on perovskite films, which showed much longer cell lifetime under 1 Sun illumination with continuous maximum power output.

As featured in:

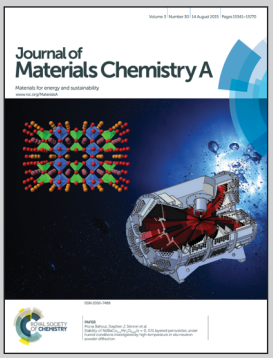

See Yabing Qi *et al.*, *J. Mater. Chem. A*, 2015, **3**, 15451.

ROYAL SOCIETY OF CHEMISTRY

www.rsc.org/MaterialsA

Registered charity number: 207890

Journal of Materials Chemistry A

PAPER

View Article Online
View Journal | View Issue

Cite this: J. Mater. Chem. A, 2015, 3, 15451

Pinhole-free hole transport layers significantly improve the stability of $MAPbI_3$-based perovskite solar cells under operating conditions†

Luis K. Ono,‡ Sonia R. Raga,‡ Mikas Remeika, Andrew J. Winchester, Atsushi Gabe and Yabing Qi*

Received 11th May 2015
Accepted 9th June 2015

DOI: 10.1039/c5ta03443d

www.rsc.org/MaterialsA

Pinhole-free 2,2′,7,7′-tetrakis(*N*,*N*-di-*p*-methoxyphenylamine)-9,9′-spirobifluorene (spiro-MeOTAD) hole transport layers (HTLs) were deposited on perovskite films. $MAPbI_3$-based perovskite solar cells employing the pinhole-free HTL showed a prolonged lifetime under one sun and was operated at the maximum power point. The solar cell architecture (planar *versus* mesoporous-layers) was also observed to strongly influence the cell's stability.

Organo-lead-halide perovskite (OHP) based solar cells are the new solar cells that hold promise for large-scale solar-to-electricity conversion at low-cost. Since the first few reports,[1–4] optimization of perovskite synthesis and device architecture has led to power conversion efficiencies (PCEs) as high as 20.1% in just a few years.[5–7] Compatibilities with flexible substrates and solution-based fabrication processes such as ultra-sonic spray-coating[8] and printing technology[9,10] make OHP cell technology amenable to scaling up to production levels.

Methylammonium (MA) lead halide (*e.g.* $CH_3NH_3PbI_3$), the most commonly employed material in OHP solar cells, was reported to have high absorption coefficients (direct bandgap ~1.55 eV) as well as high mobilities for electrons and holes, resulting in long carrier diffusion lengths (100 nm to 1 μm).[11,12] On the other hand, only a few studies provided data on the lifetime and degradation mechanisms of the fabricated OHP-based solar cells under operating conditions (*e.g.* under light and cells operated at the maximum power point – MPP). Based on these studies, ambient air/moisture, temperature and light exposure can lead to the degradation of perovskite solar cells.[13–16] It is also found that a suitable choice of top electron- or hole-transport layers (ETL and HTL) on top of the perovskite layer as well as the top-electrode contacts (*e.g.* Au, Ag, Al, *etc.*) may help protect the active layer.[17–23] 2,2′,7,7′-Tetrakis(*N*,*N*-di-*p*-methoxyphenylamine)-9,9′-spirobifluorene (spiro-MeOTAD) is the most widely used HTL in high performance OHP cells.[3,6,24] Issues have been reported regarding the spiro-MeOTAD HTL such as strong influence of air exposure on conductivity and interface energy level variations.[20,21,25] Recently our group found that the as-prepared spiro-MeOTAD films using spin-coating show a high density of pinholes (small sized pinholes ~4 pinholes per μm^2 with a diameter of ~135 nm and large sized pinholes ~289 pinholes per mm^2 with diameters in the range of 1–20 μm).[21] The formation of pinholes is characteristic of the spin-coating process of the spiro-MeOTAD compound using chlorobenzene as a solvent. Additional cross-sectional view scanning electron microscopy (SEM) measurements revealed that these pinholes form channels across the film thickness (~240 nm). These pinholes are expected to facilitate the inward diffusion of gas molecules present in ambient air (*e.g.* H_2O and O_2) leading to detrimental effects on the underneath perovskite layer. In addition, these pinholes can also facilitate the outward diffusion of chemical elements/compounds with high vapor pressure such as iodine-containing volatile species (MAI and/or HI) as a result of the degradation and/or decomposition of the $CH_3NH_3PbI_3$ perovskite film. Moreover, the pinholes in the spiro-MeOTAD HTL are possibly the cause of the aging-induced shunting pathway formation, which leads to reduced device performance.[26]

In this work, we report on a convenient methodology for preparing pinhole-free spiro-MeOTAD HTLs by changing the solvent from the commonly used chlorobenzene to chloroform. The cells with a pinhole-free spiro-MeOTAD HTL using chloroform as a solvent were able to generate power conversion efficiencies (PCEs) similar to the cells with a HTL prepared using chlorobenzene as a solvent. To minimize the influence of hysteresis behaviors that were observed in both cells, we have taken caution to determine the steady-state PCEs, which are obtained by analyzing the time-dependent photocurrent signal

Energy Materials and Surface Sciences Unit (EMSS), Okinawa Institute of Science and Technology Graduate University (OIST), 1919-1 Tancha Onna-son, Okinawa 904-0495, Japan. E-mail: Yabing.Qi@OIST.jp

† Electronic supplementary information (ESI) available: Experimental section; SEM, XRD and UV-vis characterization; steady-state PCE, j_{sc}, V_{oc}, and FF profiles and solar cell electrical output profiles corresponding to the MPP of individual cells; relative humidity and temperature profiles; solar cell parameters of the Si cell mounted adjacent to the perovskite cell. See DOI: 10.1039/c5ta03443d

‡ These authors contributed to this work equally.

using staircase voltage sweep measurements.[27] The stability of the cells was compared under operating conditions, *i.e.* with continuous illumination (AM1.5G) and applied bias tracking the maximum power point, simulating the real operation, and in a controlled environment of air with a relative humidity of ~42%. The stability measurement procedure adopted here corresponds to the ISOS-L-1 protocol.[18] We observed a prolonged lifetime of more than 10 times for the cells using the HTL prepared by using chloroform. In this work, we use the T80 parameter, defined as the time taken by a solar cell to decay 20% from the initial PCE, to quantify the lifetime in our solar cells.[28] T80 values of ~2.6 hours and ~28 hours were obtained for the sample prepared by using chlorobenzene and chloroform, respectively.

In this work, perovskite films were deposited on fluorine-doped tin oxide/blocking-layer TiO_2/mesoporous-TiO_2 (FTO/bl-TiO_2/mp-TiO_2) using PbI_2 and MAI precursors, by a modified two-step sequential deposition method.[24] Sample preparation details are described in the ESI.† Perovskite film characterization by SEM, X-ray diffraction (XRD), and UV-vis spectroscopy is shown in ESI Fig. S1.† The as-prepared perovskite films present characteristic XRD peaks at 14.1°, 28.4° and 43.2° corresponding to the (110), (220) and (330) orthorhombic crystal structure.[24] SEM images show a uniform layer completely covering the mesostructured TiO_2 film, with perovskite crystal domains in the range of 50–100 nm. The onset in the absorbance of the perovskite film in the UV-vis scan gives an optical band gap of 1.58 eV. Additional atomic force microscopy (AFM), SEM, and X-ray photoelectron spectroscopy (XPS) measurements (Fig. 1a–e) were performed on the complete device, which confirm the characteristic pinholes in the spiro-MeOTAD films prepared by using chlorobenzene (named ClB cells) and pinhole-free films by changing the solvent to chloroform (named ClF cells hereafter). Voids were also observed on Au top electrodes only on ClB cells, reflecting the spiro-MeOTAD film morphology underneath Au electrodes (Fig. 1c–d). XPS measurements conducted after the stability tests revealed the presence of a larger amount of iodine-containing compounds on the top surface of ClB cells, which are directly correlated with the observed pinholes (Fig. 1a and c) and will be described in more detail.

All freshly fabricated $MAPbI_3$-based solar cells had the characteristic dark-brownish color (Fig. 1f) and were initially tested in an Oriel solar simulator (AM1.5G) in air for the screening process (Fig. S2†). The cells with PCE over 10% were subsequently loaded in a home-designed environmental chamber coupled with a solar simulator (Peccell PEC-L01, AM1.5G) and source meters (Keithley 2401) controlled by a LabView program, allowing automatic measurements of twenty four cells with adjustable time intervals. In addition to stability testing, this setup is also capable of transient photocurrent measurements (Fig. 2).[27,29–31] The champion cell (Fig. S2†) in the ClB cell batch (presence of pinholes, Fig. 1a) generated an open-circuit voltage (V_{oc}), short-circuit current (j_{sc}), fill factor (FF), and PCE of 1.047 V, 19.7 mA cm^{-2}, 0.72, and 14.9%, respectively. The measurements were taken with a voltage scan of 0.37 V s^{-1} in the reverse direction (1.15 V → −0.1 V) under standard AM1.5G illumination. The top performing cell in ClF cells

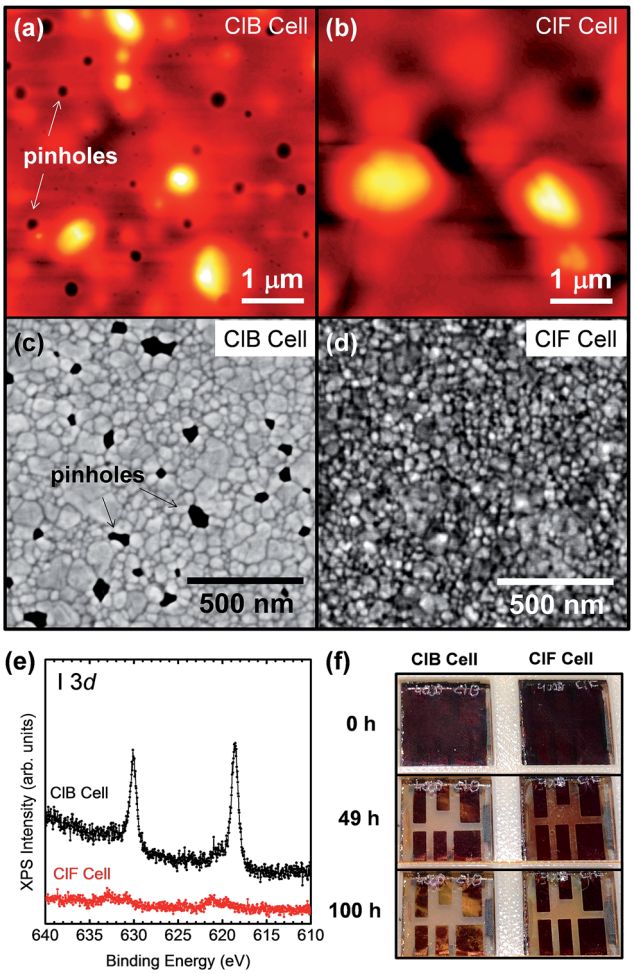

Fig. 1 (a and b) Tapping mode AFM topography images, (c and d) SEM images acquired on Au electrodes, and (e) post-mortem XPS spectra (Al-Kα = 1486.6 eV) corresponding to the I 3*d* core level of the ClB and ClF cells measured after the 102 hours stability test. (f) Optical micrographs of solar cell devices monitored during the stability test under ambient air with 42% relative humidity.

(pinhole-free HTL, Fig. 1b) showed a V_{oc}, j_{sc}, FF, and PCE of 1.036 V, 19.7 mA cm^{-2}, 0.56, and 11.4%, respectively. The lower fill factor and PCE of the cell using a chloroform-based HTL are mainly due to an increase in series resistance, which is attributed to a slower "air-induced dopant redistribution"[21] of the spiro-MeOTAD layer in the absence of pinholes. As reported in previous studies, the air exposure step after the spin-coating of the spiro-MeOTAD layer before the top contact evaporation is essential for achieving optimal efficiencies.[25]

The selected cells from the screening process were loaded into the stability setup and the steady-state solar cell parameters (PCE, j_{sc}, V_{oc}, and FF) were acquired every two hours. Note that during the waiting time (*i.e.* when not under the transient measurements) an active bias voltage was applied to the cells maintaining the solar cell operation at their MPP. Typical transient photocurrent signals are shown in Fig. 2a. This time-dependent behavior was previously explained as being caused by capacitive currents in the perovskite solar cells.[27,29–32] Such

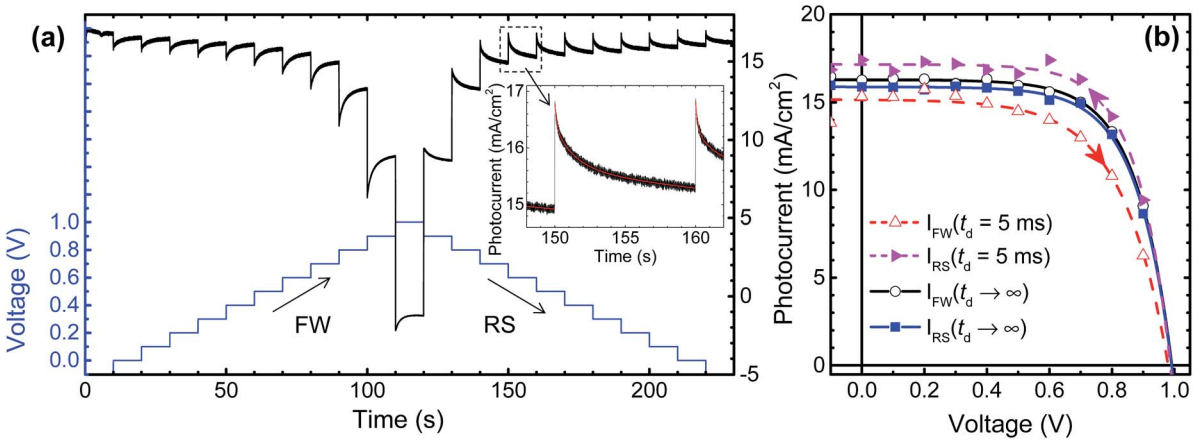

Fig. 2 (a) Time-dependent photocurrent signal as a function of applied voltage in $MAPbI_3$-based perovskite (ClB cell) using a staircase function generator. The voltage sweep from negative to positive voltage and from positive to negative is denoted as forward (FW) and reverse (RS), respectively. The 10 s long step delayed photocurrent responses were measured under AM1.5G illumination. The steep jumps observed in the current signals after each step-voltage are signatures of the capacitive effects in the device, inset in (a). (b) Current *versus* voltage curves composed from the time-dependent data shown in (a) considering 5 ms delay time (t_d) and steady state conditions ($t_d \rightarrow \infty$).

capacitance effects were hypothesized to be originated from (i) ferroelectricity or polarization of the perovskite layer, (ii) ion migration (iii) trapping/de-trapping of charge carriers, and/or (iv) capacitive effects in the selective-contacts (ETL and HTL).[27,29–33] The procedures for extracting the steady-state *I–V* curves are based on multi-term exponential fitting (inset in Fig. 2a), which have been described in detail elsewhere.[27] To make a convention for this work, we set the voltage sweep starting from the negative to the positive voltage (direction from j_{sc} to V_{oc}) to be the forward (FW) scan direction, and the voltage starting from positive to negative (direction from V_{oc} to j_{sc}) to be the reverse (RS) scan direction. The *I–V* curves shown in Fig. 2b were generated from the time-dependent data (Fig. 2a) considering 5 ms delay time (t_d) and steady state conditions ($t_d \rightarrow \infty$). A better overlapping in FW and RS *I–V* curves is observed when calculating the steady state conditions ($t_d \rightarrow \infty$). The *I–V* curves of our $MAPbI_3$-based solar cells exhibit hysteresis effects when the voltage sweep is fast. Studies have shown that PCE should be extracted when the efficiencies of the FW and RS scans coincide.[27,29–31] In the particular case of the *I–V* curves shown in Fig. 2b, steady state PCE values of 11.7% and 11.4% were extracted in FW and RS scan directions, respectively. Meanwhile, considering a fast sweeping of $t_d = 5$ ms, two substantially different PCE values of 10.6% and 12% were extracted corresponding to FW and RS scans, respectively. Thus, an increase by ~10% in efficiency is observed in the FW direction when steady state conditions ($t_d \rightarrow \infty$) are measured and compared to *I–V* curves measured at a fast scan speed ($t_d = 5$ ms). On the other hand, a decrease by ~5% in efficiency is observed in the RS direction when steady state *I–V* curves are measured and compared to *I–V* scanned at faster rates. This means that, when the *I–V* curves are measured at faster scan rates, PCE values are underestimated and overestimated when under the forward and reverse directions, respectively. Although the measured PCEs under steady state conditions can be sometimes substantially lower than the ones measured at a fast scan speed in the reverse direction, they represent more accurately the realistic device performance.

The evolution of steady-state solar cell performance parameters (PCE, j_{sc}, V_{oc}, and FF) was monitored over ~102 h in ambient air (Fig. 3). The transient photocurrent signals were measured every two hours. The stability profiles are based on statistical analysis from at least five cells. Solar cell parameters as well as electrical outputs from individual cells are shown in Fig. S3–S6.† Temperature and humidity profiles under which the cells were measured are shown in Fig. S7.† Any change of the light intensity over time was monitored using an additional Si solar cell mounted adjacent to the perovskite cells. As shown in Fig. S8,† changes in light intensity were negligible (<1% in PCE) over the 102 h measurement period. When $MAPbI_3$ cells were operated in air, a fast and continuous decrease in PCE was observed for ClB cells. All ClB cells yielded a PCE of 0% after 12 hours continuous operation at the MPP. On the other hand, ClF cells show significantly better stability: decreased by only ~12% from the initial PCE during the first 12 hours. To provide a more standardized way for quantifying lifetime, we have adopted the T80 parameter (time interval corresponding to the first 20% decay in PCE) defined by Krebs and co-workers.[18,28] T80 values of ~2.6 hours and ~28 hours were extracted from the stability profile (Fig. 3) of ClB and ClF cells, respectively. After ~100 hour operation, the ClF cells decreased by ~50% in PCEs. The PCE profile is reflected in the interplay of j_{sc}, V_{oc}, and FF profiles. Because the perovskite-based solar cell structure is complex (FTO/bl-TiO_2/mp-TiO_2/$MAPbI_3$/spiro-MeOTAD/Au), convoluted physico-chemical changes in each layer are expected to affect the overall j_{sc}, V_{oc}, and FF profiles. The decay in j_{sc} observed in the ClB sample can be attributed mainly to the degradation of the $MAPbI_3$ absorbing layer generating less photocurrent as a function of operation time. XRD (Fig. S1c†) confirms that the perovskite crystalline peak disappears in ClB cells after the ~100 hour operation. The degradation of the perovskite layer is proposed to be induced by the reaction with H_2O (moisture) in

an atmosphere generating MA, MAI, PbI_2, and HI as final products.[13,15,34,35] Furthermore, it has been reported that HI and MA have boiling temperatures of −35.4 °C and −6 °C at room temperature, respectively; thus, they are present mainly in the gas phase.[15] A linear-type decay is observed for the monitored ~100 hour stability profile in the ClF cells. As described above, AFM images (Fig. 1a and b) show distinctly different morphologies for the spiro-MeOTAD regions (between Au electrodes) of ClB and ClF cells. A high density of pinholes is observed on ClB cells and expected to promote the inward diffusion of H_2O and O_2 gas molecules present in ambient air degrading the $MAPbI_3$ active material as well as the outward diffusion of degradation products having high vapor pressure such as MAI and/or HI. These descriptions are corroborated by the post-mortem XPS measurements (Fig. 1e), XRD measurements (Fig. S1c†), and the distinct color changes during aging (Fig. 1f). A large amount of iodine-containing compounds (most likely MAI) was detected by XPS on the top surface of ClB cells. Interestingly, although much less than that on the ClB cells, the ClF cells also showed that some iodine species were present on the top surface meaning that the pinhole-free spiro-MeOTAD layer is still not able to completely stop the diffusion. The slower diffusion of moisture through the pinhole-free spiro-MeOTAD layer may lead to a slow PCE decrease profile. Visual inspection (Fig. 1f) of the cells also confirms the stronger bleaching on the ClB cell between Au electrodes as well as yellow-colored spots under the Au electrodes. On the other hand, on the ClF cells, the dark-brownish color is maintained in the areas under the Au electrodes. This indicates that the combination of the pinhole-free spiro-MeOTAD layer and the top Au electrode helps protect the underneath $MAPbI_3$ by effectively slowing down the diffusion of moisture and O_2 inward. Thus, the perovskite degradation is expected to be slowed down by the use of an efficient gas-barrier encapsulating material.

To simulate the conditions that are similar to a suitable encapsulation layer, we have taken the approach of conducting the aging tests in a N_2 atmosphere with the aid of the environmental chamber, which allows us to find a perovskite-architecture with enhanced stability as the first step. We have studied the stability of several solar cell structures (planar *versus* mesoporous-layer) as shown in Fig. 4. The FTO/c-TiO_2/mp-Al_2O_3 + $MAPbI_3$/spiro-MeOTAD (chloroform)/Au devices despite the initial lower efficiencies (~6.5%) outperformed in stability (Fig. 4 and S9–S10†). The cell temperatures were constant at ~65–70 °C during the ~100 hour stability test. The device architectures (*e.g.* planar *versus* incorporation of a mesoporous-

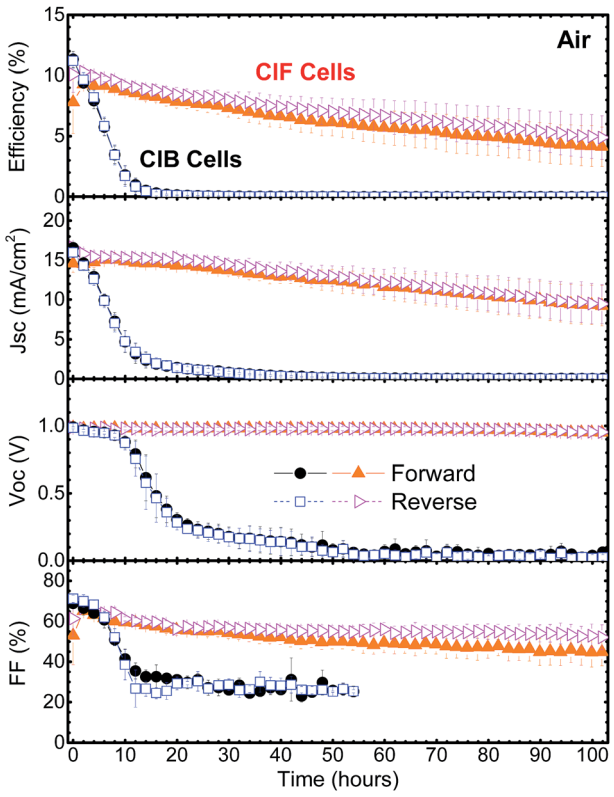

Fig. 3 Stability profile of the FTO/bl-TiO_2/mp-TiO_2/$MAPbI_3$/spiro-MeOTAD/Au perovskite solar cell with spiro-MeOTAD dissolved in chlorobenzene (ClB cells) and chloroform (ClF cells) operated under air with a controlled relative humidity of ~42%. When the cells were not under the *I*–*V* measurements, a constant voltage was supplied to the cells matching the voltage at the maximum power point. The steady-state efficiency, short circuit current (j_{sc}), open-circuit voltage (V_{oc}), and fill factor (FF) were calculated based on statistical analysis from at least five different cells.

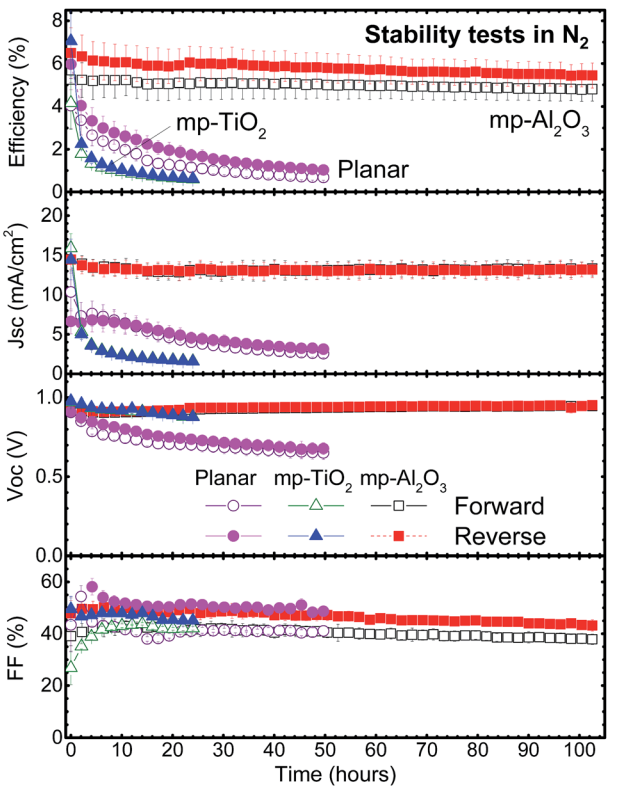

Fig. 4 Stability profile (PCE, j_{sc}, V_{oc}, and FF) of FTO/bl-TiO_2/$MAPbI_3$/spiro-MeOTAD (chloroform)/Au (triangles), FTO/bl-TiO_2/mp-TiO_2/$MAPbI_3$/spiro-MeOTAD (chloroform)/Au (circles), and FTO/bl-TiO_2/mp-Al_2O_3/$MAPbI_3$/spiro-MeOTAD (chloroform)/Au (squares) perovskite solar cells under N_2 (0% relative humidity).

layer) as well as material choices are expected to influence the cell stability. Enhanced long-term solar cell operational stability was achieved using mp-Al_2O_3 instead of the commonly employed planar and/or mp-TiO_2, an ultraviolet-active photocatalytic material.[22,26] The lower PCE in our cell seems to be correlated with the top spiro-MeOTAD layer. Spiro-MeOTAD in its pristine form suffers from low conductivity. Thus, inclusion of a dopant (*e.g.*, LiTFSI) is a common practice and essential to promote the redistribution of dopants, increasing conductivity. However, for further enhancement of the conductivity in these doped-spiro-MeOTAD films, ambient air exposure is needed and generally correlated with spatial redistribution of LiTFSI dopants in spiro-MeOTAD films.[25,36–38] In this sense, in the time frame of typically a few hours, the presence of pinholes is beneficial to achieve uniform doping across the spiro-MeOTAD film thickness. Thus, conductivity in doped-spiro-MeOTAD films is easily influenced by the film morphology and gas exposure leading ultimately to variations in solar cell performances reported.[25,36–38] The fabrication of stable perovskite solar cells based on air exposure induced doping is difficult to control. Additional solutions of the spiro-MeOTAD HTL dissolved in different chlorobenzene : chloroform mixed solvents were studied (see detailed description in Fig. S12†). AFM images showed aggregates and/or crystallization when mixed chlorobenzene : chloroform solvents were used to dissolve spiro-MeOTAD, Li-TFSI and *t*-BP. On the basis of our study, in order to avoid influence from ambient air on the perovskite solar cell parameters by using encapsulation, it is essential to tackle strategically the top doped-spiro-MeOTAD layer such as the use of chemical dopants where it allows better doping control without the influence of air exposure.[39,40] Alternative inorganic based HTLs, such as CuI, CuSCN, Cs_2SnI_6, and NiO_x, are of interest and are being currently tested for their influence on the stability of perovskite-based solar cells.[41–46]

In summary, we have demonstrated a simple methodology for generating pinhole-free spiro-MeOTAD HTLs by changing the chlorobenzene solvent to chloroform when dissolving the spiro-MeOTAD powder. The steady-state solar cell parameters (PCE, J_{sc}, V_{oc}, and FF) as a function of time were measured. The stability profile of the pinhole-free cells (using chloroform as a solvent) outperformed the pinhole cells (using chlorobenzene as a solvent) under operation conditions (under continuous illumination with AM1.5G and applied bias tracking the maximum power point in a controlled environment of air with a relative humidity of 42%). Furthermore, we showed that $MAPbI_3$-based perovskite solar cells employing the mesostructured Al_2O_3 layer showed long-term stability when operated in a dry N_2 environment. Our study shows the potential of OHP cells for commercial deployment as new photovoltaic technology when appropriate HTL and encapsulation materials are employed.

Acknowledgements

This work was supported by funding from the Energy Materials and Surface Sciences Unit of the Okinawa Institute of Science and Technology Graduate University.

References

1 A. Kojima, K. Teshima, Y. Shirai and T. Miyasaka, *J. Am. Chem. Soc.*, 2009, **131**, 6050–6051.
2 J.-H. Im, C.-R. Lee, J.-W. Lee, S.-W. Park and N.-G. Park, *Nanoscale*, 2011, **3**, 4088–4093.
3 H. S. Kim, C. R. Lee, J. H. Im, K. B. Lee, T. Moehl, *et al.*, *Sci. Rep.*, 2012, **2**, 591.
4 M. M. Lee, J. Teuscher, T. Miyasaka, T. N. Murakami and H. J. Snaith, *Science*, 2012, **338**, 643–647.
5 National Renewable Energy Laboratory (NREL), http://www.nrel.gov/ncpv/images/efficiency_chart.jpg.
6 H. Zhou, Q. Chen, G. Li, S. Luo, T.-B. Song, *et al.*, *Science*, 2014, **345**, 542–546.
7 N. J. Jeon, J. H. Noh, W. S. Yang, Y. C. Kim, S. Ryu, J. Seo and S. I. Seok, *Nature*, 2015, **517**, 476–480.
8 A. T. Barrows, A. J. Pearson, C. K. Kwak, A. D. F. Dunbar, A. R. Buckley and D. G. Lidzey, *Energy Environ. Sci.*, 2014, **7**, 2944–2950.
9 A. Mei, X. Li, L. Liu, Z. Ku, T. Liu, *et al.*, *Science*, 2014, **345**, 295–298.
10 K. Hwang, Y.-S. Jung, Y.-J. Heo, F. H. Scholes, S. E. Watkins, J. Subbiah, D. J. Jones, D.-Y. Kim and D. Vak, *Adv. Mater.*, 2015, **27**, 1241–1247.
11 C. Wehrenfennig, M. Z. Liu, H. J. Snaith, M. B. Johnston and L. M. Herz, *Energy Environ. Sci.*, 2014, **7**, 2269–2275.
12 H. S. Jung and N. G. Park, *Small*, 2015, **11**, 10–25.
13 G. Niu, X. Guo and L. Wang, *J. Mater. Chem. A*, 2015, **3**, 8970–8980.
14 R. K. Misra, S. Aharon, B. Li, D. Mogilyansky, I. Visoly-Fisher, L. Etgar and E. A. Katz, *J. Phys. Chem. Lett.*, 2015, **6**, 326–330.
15 Y. Han, S. Meyer, Y. Dkhissi, K. Weber, J. M. Pringle, U. Bach, L. Spiccia and Y.-B. Cheng, *J. Mater. Chem. A*, 2015, **3**, 8139–8147.
16 L. K. Ono, S. Wang, Y. Kato, S. R. Raga and Y. B. Qi, *Energy Environ. Sci.*, 2014, **7**, 3989–3993.
17 M. Jorgensen, K. Norrman and F. C. Krebs, *Sol. Energy Mater. Sol. Cells*, 2008, **92**, 686–714.
18 M. O. Reese, S. A. Gevorgyan, M. Jorgensen, E. Bundgaard, S. R. Kurtz, *et al.*, *Sol. Energy Mater. Sol. Cells*, 2011, **95**, 1253–1267.
19 S. Ryu, J. Seo, S. S. Shin, Y. C. Kim, N. J. Jeon, J. H. Noh and S. I. Seok, *J. Mater. Chem. A*, 2015, **3**, 3271–3275.
20 L. K. Ono, P. Schulz, J. J. Endres, G. O. Nikiforov, Y. Kato, A. Kahn and Y. B. Qi, *J. Phys. Chem. Lett.*, 2014, **5**, 1374–1379.
21 Z. Hawash, L. K. Ono, S. R. Raga, M. V. Lee and Y. B. Qi, *Chem. Mater.*, 2015, **27**, 562–569.
22 T. Leijtens, G. E. Eperon, S. Pathak, A. Abate, M. M. Lee and H. J. Snaith, *Nat. Commun.*, 2013, **4**, 2885.
23 M. Seetharaman, S. P. Nagarjuna, P. N. Kumar, S. P. Singh, M. Deepa and M. A. G. Namboothiry, *Phys. Chem. Chem. Phys.*, 2014, **16**, 24691–24696.
24 J. Burschka, N. Pellet, S. J. Moon, R. Humphry-Baker, P. Gao, M. K. Nazeeruddin and M. Gratzel, *Nature*, 2013, **499**, 316–319.

25 U. B. Cappel, T. Daeneke and U. Bach, *Nano Lett.*, 2012, **12**, 4925–4931.
26 S. Guarnera, A. Abate, W. Zhang, J. M. Foster, G. Richardson, A. Petrozza and H. J. Snaith, *J. Phys. Chem. Lett.*, 2015, **6**, 432–437.
27 L. K. Ono, S. R. Raga, S. Wang, Y. Kato and Y. B. Qi, *J. Mater. Chem. A*, 2015, **3**, 9074–9080.
28 M. Jorgensen, K. Norrman, S. A. Gevorgyan, T. Tromholt, B. Andreasen and F. C. Krebs, *Adv. Mater.*, 2012, **24**, 580–612.
29 H. J. Snaith, A. Abate, J. M. Ball, G. E. Eperon, T. Leijtens, *et al.*, *J. Phys. Chem. Lett.*, 2014, **5**, 1511–1515.
30 H.-S. Kim and N.-G. Park, *J. Phys. Chem. Lett.*, 2014, **5**, 2927–2934.
31 E. L. Unger, E. T. Hoke, C. D. Bailie, W. H. Nguyen, A. R. Bowring, T. Heumuller, M. G. Christoforo and M. D. McGehee, *Energy Environ. Sci.*, 2014, **7**, 3690–3698.
32 W. Tress, N. Marinova, T. Moehl, S. M. Zakeeruddin, M. K. Nazeeruddin and M. Gratzel, *Energy Environ. Sci.*, 2015, **8**, 995–1004.
33 H. W. Chen, N. Sakai, M. Ikegami and T. Miyasaka, *J. Phys. Chem. Lett.*, 2015, **6**, 164–169.
34 G. D. Niu, W. Z. Li, F. Q. Meng, L. D. Wang, H. P. Dong and Y. Qiu, *J. Mater. Chem. A*, 2014, **2**, 705–710.
35 J. Yang, B. D. Siempelkamp, D. Liu and T. L. Kelly, *ACS Nano*, 2015, **9**, 1955–1963.
36 P. Docampo, S. Guldin, T. Leijtens, N. K. Noel, U. Steiner and H. J. Snaith, *Adv. Mater.*, 2014, **26**, 4013–4030.
37 A. Abate, T. Leijtens, S. Pathak, J. Teuscher, R. Avolio, *et al.*, *Phys. Chem. Chem. Phys.*, 2013, **15**, 2572–2579.
38 L. Yang, B. Xu, D. Q. Bi, H. N. Tian, G. Boschloo, L. C. Sun, A. Hagfeldt and E. M. J. Johansson, *J. Am. Chem. Soc.*, 2013, **135**, 7378–7385.
39 W. H. Nguyen, C. D. Bailie, E. L. Unger and M. D. McGehee, *J. Am. Chem. Soc.*, 2014, **136**, 10996–11001.
40 J. Burschka, A. Dualeh, F. Kessler, E. Baranoff, N. L. Cevey-Ha, C. Y. Yi, M. K. Nazeeruddin and M. Gratzel, *J. Am. Chem. Soc.*, 2011, **133**, 18042–18045.
41 P. Qin, S. Tanaka, S. Ito, N. Tetreault, K. Manabe, H. Nishino, M. K. Nazeeruddin and M. Gratzel, *Nat. Commun.*, 2014, **5**, 3834.
42 J. A. Christians, R. C. M. Fung and P. V. Kamat, *J. Am. Chem. Soc.*, 2014, **136**, 758–764.
43 A. S. Subbiah, A. Halder, S. Ghosh, N. Mahuli, G. Hodes and S. K. Sarkar, *J. Phys. Chem. Lett.*, 2014, **5**, 1748–1753.
44 L. Hu, J. Peng, W. Wang, Z. Xia, J. Yuan, *et al.*, *ACS Photonics*, 2014, **1**, 547–553.
45 S. Chavhan, O. Miguel, H.-J. Grande, V. Gonzalez-Pedro, R. S. Sanchez, E. M. Barea, I. Mora-Sero and R. Tena-Zaera, *J. Mater. Chem. A*, 2014, **2**, 12754–12760.
46 B. Lee, C. C. Stoumpos, N. Zhou, F. Hao, C. Malliakas, C.-Y. Yeh, T. J. Marks, M. G. Kanatzidis and R. P. H. Chang, *J. Am. Chem. Soc.*, 2014, **136**, 15379–15385.